11th International Workshop on Ship and Marine Hydrodynamic
Hamburg, Germany, September 22-25, 2019

Wave-Induced Motions of Moored and Coupled Multi-Body Offshore Structures

G. Seithe[1,*], O. el Moctar[1]

[1]University of Duisburg-Essen, Institute of Ship Technology, Ocean Engeneering and Transport Systems (ISMT)
Bismarckstrae 69, 47057 Duisburg, Germany

[*]Corresponding author, grusche.seithe@uni-due.de

ABSTRACT

In the recent past, very large floating structures (VLFS) are used to realize a variety of large marine facilities like floating piers, bridges or logistical hubs, substituting the traditional bottom mounted structures. In most cases VLFSs consist of a number of individual modules that are assembled with connectors and hold in place by mooring systems. To ensure proper working and safety conditions, their hydrodynamic response in different sea states needs to be investigated. Previous investigations relied mainly on potential flow solvers which do not account for viscous and other nonlinear effects. However, flow properties under severe conditions are highly nonlinear. To capture the physics of such phenomena field methods are the preferred choice. The present work aims to investigate the hydrodynamic response of such a moored and coupled multi-body VLFS in waves using a flow code that computes multiphase unsteady incompressible flow simulations using the Navier Stokes equations coupled with a six-degrees-of-freedom (6 DOF) multi-body solver and mooring model. A total number of 14 simulations have been conducted for single and multiple cuboid set-ups. The set-ups are based on the model tests performed at TU Delft. The hydrodynamic responses were assessed and show a favourable comparison for most cases between the computed and measured results.

1 INTRODUCTION

Recently, a variety of large marine facilities, very large floating structures (VLFSs) have been proposed as an alternative to bottom mounted structures. The main advantage of such floating solutions is their reduced environmental impact and higher installation and transport flexibility because deep water foundations are no longer critical. To ensure proper working and safety conditions, their hydrodynamic response in different sea states needs to be investigated. Already several possible applications of VLFSs, such as floating breakwaters [1–3], water level carpets [4], floating piers [5], floating airports [6] and floating bridges [7, 8] were analysed to predict hydrodynamic and hydro elastic responses. These investigations relied mainly on potential flow solvers which do not account for viscous and other nonlinear effects. However, flow properties under severe conditions are highly nonlinear, brought about by breaking waves and effects of water on deck, slamming, hydrodynamic damping and shallow water. To capture the physics of such phenomena, viscous field methods are the preferred choice.

A VLFS consists of a number of smaller coupled and moored pontoons. The present work aims to investigate the hydrodynamic response of such a moored and coupled multi bodied VLFS in waves using a flow code that solves unsteady incompressible multiphase flows using the Navier Stokes equations coupled with a 6 DOF multi-body solver and mooring model. The platforms to be investigated consist of one, two and three connected and moored cuboid shaped rigid pontoons and hinge connections. The

mooring consist of four spring-like horizontal mooring legs attached to the bodies. The set-up is based on the model tests performed at TU Delft. Comparable numerical simulations are to be validated against model test measurements. The focus of this study lies on the pressure dominated multi-body response of the system and serves as a pre-study for future viscous investigations.

The paper gives an overview of the theoretical background used for the simulations, the experimental and numerical set ups. Thereafter, the results of the single, double and multi-body cases are presented and discussed. Finally the conclusions drawn from this work are presented and an outlook is given for further work.

2 THEORETICAL BACKGROUND

The applied method for the computational fluid dynamics solves the Navier Stokes equations using a finite volume approach. The solution domain is subdivided in control volumes, in which the Navier Stokes equations are solved in integral form.

2.1 Fluid dynamics

The description of the numerical fluid dynamics methods are restricted to major features; details may be found in [9]. The equation of mass and momentum in their integral form serve as a starting point.

$$\frac{\partial}{\partial t}\int_V \rho dV + \int_S \rho \boldsymbol{u}\cdot\boldsymbol{n}dS = 0, \tag{1}$$

$$\frac{\partial}{\partial t}\int_V \boldsymbol{u}dV + \int_S \boldsymbol{u}\boldsymbol{u}\cdot\boldsymbol{n}dS = \frac{-1}{\rho}\int_S p\cdot\boldsymbol{n}dS + \nu\int_S\left(\nabla\boldsymbol{u} + (\nabla\boldsymbol{u})^T\right)\cdot\boldsymbol{n}dS + \frac{1}{\rho}\int_V \boldsymbol{f}dV \tag{2}$$

The vector $\boldsymbol{u}$ describes the fluid velocity, p and ρ are the pressure and the constant fluid density whereas ν and $\boldsymbol{f}$ donate the kinematic viscosity and the volume force. S describes the surface of the control volume V with its outward pointing normal vector $\boldsymbol{n}$. As the fluid is considered to be inviscid within this study the equations above take the Eulerian form without viscosity.

The solution domain is subdivided into a finite number of control volumes which may be of arbitrary shape. Integrals are numerically approximated using the midpoint rule. The mass flux through a cell face is taken from the previous iteration. No explicit equation to solve the pressure term is directly available. Hence, it is necessary to derive a pressure-velocity correction equation. The coupling between pressure and velocity is given in the SIMPLE- (Semi Implicit Method of Pressure Linked Equations) algorithm. To fulfil the conservation equations, the pressure and velocities are iteratively corrected for each time instant within the algorithm. Remaining unknown variables at the cell face centres are determined by combining a central differencing scheme (CDS) with an upwind differencing scheme (UDS). The blending is done to obtain a good compromise between the stability of the UDS and the accuracy of the CDS. A second order three-time-level implicit method is used to integrate in time. The system of equations is under relaxed to dampen changes between iterations. The interface between water and air is determined using the volume of fluid method (VOF). The free surface is captured by the distribution of the volume fraction c, which is 0 in air and 1 in water. For the volume fraction, an additional conservation equation is solved:

$$\frac{\partial}{\partial t}\int_V c dV + \int_S c\boldsymbol{u}\cdot\boldsymbol{n}dS = 0 \tag{3}$$

The conservation equations are solved for an effective fluid and the effective fluid density ρ_{eff} then reads:

$$\rho_{eff} = c\rho_{water} + (1-c)\,\rho_{air} \tag{4}$$

The high-resolution interface-capturing scheme (HRIC) is used to keep the transition between the two fluids sharp and to ensure the boundedness of c at the same time. The above conservation equations

are nonlinear and coupled. Residuals of an equation are reduced to a certain limit using an iterative solution procedure (inner iterations). After all equations of the system are solved, the coefficient matrices and the source vector are updated and the process is repeated (outer iterations). When a certain convergence criterion or the maximum number of outer iterations are reached, the solver continues with the next time step.

2.2 Rigid body equations of motions

The equations of motion for a single rigid body are solved in the local reference frame of the body with its origin located at the centre of gravity of the body $\boldsymbol{O}(x, y, z)$. Rotational attitude of the floating body can be described by the generalized coordinates $\boldsymbol{\alpha} = (\alpha_1, \alpha_2, \alpha_3)^T$. The rotation matrix $\boldsymbol{S}$ describes the transformation of the coordinates and forces from the local to the global reference system $\boldsymbol{O}(\xi, \eta, \zeta)$ as,

$$\boldsymbol{\xi} = \boldsymbol{\xi}_0 + \boldsymbol{S}\boldsymbol{x} \tag{5}$$

$\boldsymbol{S}$ is the result of three consecutive Euler rotations:

$$\boldsymbol{S}(\boldsymbol{\alpha}) = \boldsymbol{S}_1(\alpha_1)\,\boldsymbol{S}_2(\alpha_2)\,\boldsymbol{S}_3(\alpha_3) \tag{6}$$

The rotations used by the present method are $\boldsymbol{\alpha} = (\Psi, \Theta, \Phi)^T$, where Ψ is the rotation around the z-axis, Θ is the rotation around the y-axis and Φ around the x-axis. Therefore, the rotation matrix becomes:

$$S(\Psi, \Theta, \Phi) = \begin{bmatrix} \cos(\Psi) & -\sin(\Psi) & 0 \\ \sin(\Psi) & \cos(\Psi) & 0 \\ 0 & 0 & 1 \end{bmatrix} \begin{bmatrix} \cos(\Theta) & 0 & \sin(\Theta) \\ 0 & 1 & 0 \\ -\sin(\Theta) & 0 & \cos(\Theta) \end{bmatrix} \begin{bmatrix} 1 & 0 & 0 \\ 0 & \cos(\Phi) & -\sin(\Phi) \\ 0 & \sin(\Phi) & \cos(\Phi) \end{bmatrix} \tag{7}$$

$$= \begin{bmatrix} c\Psi c\Phi & c\Psi s\Theta s\Phi - s\Psi c\Phi & c\Psi s\Theta c\Phi + s\Psi s\Phi \\ s\Psi c\Theta & s\Psi s\Theta s\Phi + c\Psi c\Phi & s\Psi s\Theta c\Phi - c\Psi s\Phi \\ -s\Theta & c\Theta s\Phi & c\Theta c\Phi \end{bmatrix} \tag{8}$$

with: c : *cosinus* and s : *sinus*. The equations of motion for the translational motion $\boldsymbol{x}$ and the rotational motion $\boldsymbol{\omega}$ are:

$$\boldsymbol{F} = m\ddot{\boldsymbol{\xi}}_0 \tag{9}$$

$$\boldsymbol{M} = \boldsymbol{S}\boldsymbol{I}\boldsymbol{S}^T\dot{\boldsymbol{\omega}} \tag{10}$$

Where $\boldsymbol{F}$ and $\boldsymbol{M}$ are the external forces and moments acting on the body, m is the mass and $\boldsymbol{I}$ the inertia matrix of the body, expressed in the coordinate system of the body (x,y,z). More details can be found in [10, 11].
The dynamic behaviour of multiple interlinked bodies is described by the general equations of motion of the multi-body system:

$$\boldsymbol{I}^{mb}\ddot{\boldsymbol{q}} = \boldsymbol{f} \tag{11}$$

Where $\ddot{\boldsymbol{q}}$ is the vector of generalized coordinates, $\boldsymbol{f}$ is a generalized force and $\boldsymbol{I}^{mb}$ is the block diagonal matrix of the inertia matrices of the rigid bodies.

$$\boldsymbol{I}^{mb} = \begin{bmatrix} \boldsymbol{I}_1 & \cdots & 0 \\ \vdots & \ddots & \vdots \\ 0 & \cdots & \boldsymbol{I}_n \end{bmatrix} \tag{12}$$

The bodies can be linked with different types of joints which can allow translations and/or relative rotations to each other. Joints are described by certain kinematic constraints, which are expressed as a linear condition on the accelerations of the bodies:

$$\boldsymbol{J}\ddot{\boldsymbol{q}} = \boldsymbol{Q} \tag{13}$$

Where $\boldsymbol{J}$ is the Jacobian matrix of the constraint condition $\phi(\boldsymbol{q}, t) = 0$, $\ddot{\boldsymbol{q}}$ is the acceleration of the bodies and $\boldsymbol{Q}$ is an inhomogeneity. To enforce the acceleration conditions of the constraints, a constraint force is added to the system. By introducing the Lagrangian multiplier $\boldsymbol{\lambda}$ of all constraints, the workless constraint force is given by:

$$\boldsymbol{f}^c = \boldsymbol{J}^T \cdot \lambda \tag{14}$$

$\boldsymbol{\lambda}$ is sought in a way that the constraint force $\boldsymbol{f}^c$ in combination with all external forces $\boldsymbol{f}^{ext}$ that satisfies the constraints forming the constrained equation of motion of an interlinked multi-body system:

$$\boldsymbol{M}\ddot{\boldsymbol{q}} = \boldsymbol{J}^T\boldsymbol{\lambda} + \boldsymbol{f}^{ext}. \tag{15}$$

More details may be found in [12].

2.3 Modelling of mooring and hinge joints

The spring-like moorings used in the experimental tests of TU Delft are modelled by linear spring models which connect a body with the environment using an elastic force. This force is called restoring force as it acts in a way that a state of equilibrium is restored. It is given by Hookes law:

$$\boldsymbol{F}_1 = -k_s\left(\boldsymbol{r}_s - \boldsymbol{r}_{eq}\right), \tag{16}$$

$$\boldsymbol{F}_2 = -\boldsymbol{F}_1, \tag{17}$$

where:

$$\boldsymbol{r}_s = \boldsymbol{x}_1 - \boldsymbol{x}_2, \tag{18}$$

$$\boldsymbol{r}_{eq} = \frac{l_{eq}\boldsymbol{r}_s}{|\boldsymbol{r}_s|}. \tag{19}$$

Here, $\boldsymbol{x}_1$ is the attachment point of one end of the spring, $\boldsymbol{x}_2$ is the other end of the spring, l_{eq} is the relaxation length of the spring, $\boldsymbol{F}_1$ is the force acting on $\boldsymbol{x}_1$ and $\boldsymbol{F}_2$ is the reaction force acting on $\boldsymbol{x}_2$. The hinge joints are modelled as the connection of two 6 DOF bodies that move relatively to each other as part of a multi-body motion. The hinge allows a single relative rotation of the two bodies around the axis of revolution. All other relative motions are restricted.

3 EXPERIMENTAL SET-UP

Within the EU founded project Space@Sea, an extensive experimental test series was carried out by TU Delf in a towing tank, which measures 142m long, 4.22m wide and 2.5m deep (model scale values). The focus of the experimental investigation was on coupled body motions. The tests were performed at a geometrical scale of 1:70. Froude scaling laws were applied. In the following, all values are given in full scale values unless mentioned otherwise.

The test series comprises three different body shapes and different coupled body configuration. Within this work an investigation of the cuboid body set-ups is presented. The cuboids were connected by hinges and moored by horizontal linear spring-like moorings. Table 1 shows the properties of the models. A camera tracking system was used to measure the motion excitation of all bodies in six degrees of freedom. All translatory degree of freedom and yaw were assessed in a tank-fixed coordinate system. Roll and pitch are given in the respective local coordinate system of the body. A horizontal spring mooring is fixed to one body for all configurations in order to prevent the bodies to move too far from the camera system. The four mooring lines are guided through pulleys mounted on the tank walls, at the same height

Table 1: Main particulars of the floating cuboids

Desigantion	Value		
	Body 1	Body 2	Body 3
L_{pp} [m]	0.643	0.643	0.643
Height [m]	0.214	0.214	0.214
Draft [m]	0.128	0.128	0.128
Mass [kg]	53.02	53.08	53.12
COG above keel [m]	0.169	0.152	0.148
roll radius of gyration [m]	0.213	0.214	0.216
pitch radius of gyration [m]	0.228	0.211	0.238
yaw radius of gyration [m]	0.252	0.238	0.248
edge radius [mm]	5.5	5.5	5.5

as the body fixed fairleads, 20 mm above the still water surface. A right-handed coordinate system was used. The experimental set-up and sign convention of the used configurations of this work are shown in Figure 1. The order of rotation is Yaw-Pitch-Roll. More details can be found in the model test report of TU Delft [13].

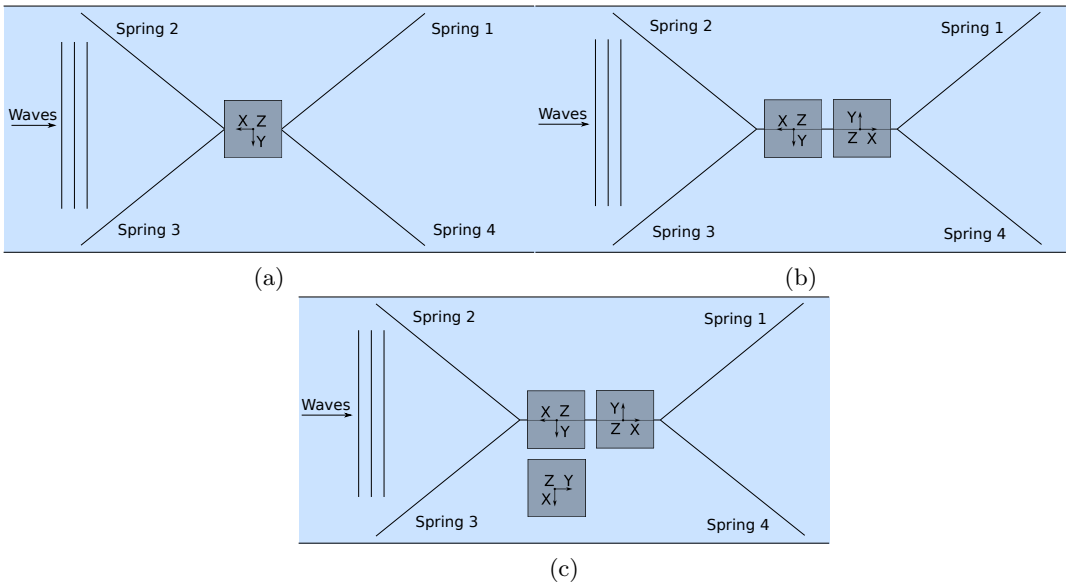

Figure 1: Experimental set-up and sign convention for single-body set up (a), double-body set-up (b) and multi-body set-up (c)

4 NUMERICAL SET-UP

All simulations were performed in model scale in accordance with the model tests. Nevertheless the results in section 5.1, section 5.2 and section 5.3 are presented in full scale dimensions for a scaling factor of 1:70 to provide a more realistic picture of the module motions. Due to the high computational cost of field method simulations the number of test cases conducted for this paper was limited to one body shape and two wave frequencies. Additionally, not all wave encounter frequencies were taken into account for the three body cases, see Table 4. For the following simulations the fluid was assumed to be inviscid as the flow is mainly pressure dominated.

Cuboids with sharp edges were used to model the bodies, neglecting the rounded edges of the bodies used in the model tests. This is considered not have a major influence on the motions.

The size of the computational domain in wave propagation direction was chosen to avoid flow disturbances at the outer boundaries. The dimensions are given relative to the wave length λ. The inlet boundary is located at a distance of 2.5λ from the closest point of the cuboid to the inlet of the domain. Whereas the outlet boundary is located at 3.5λ from the closest point of the cuboid to the outlet. The domain sides, and bottom are located at 2 meters from the cuboid's centre line. The top is located 1 meter above the still water line (see Figure 2). A wave forcing zone of 1λ is implemented at the inlet and 2.5λ at the outlet.

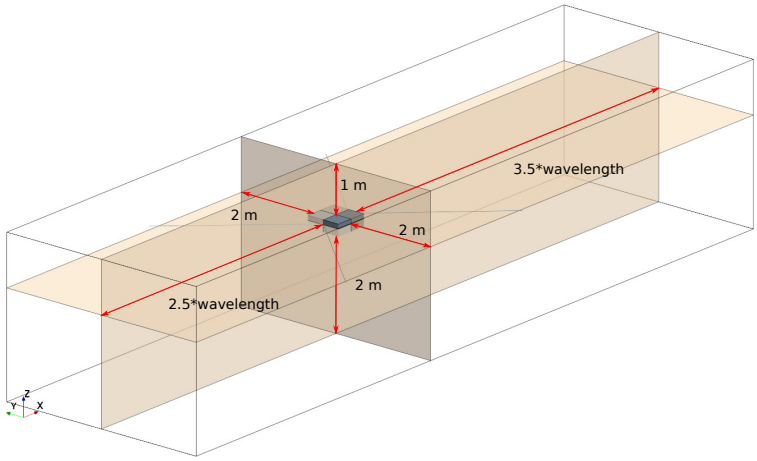

Figure 2: Dimensions of the computational domain

4.1 Coordinate systems

Two types of coordinate systems are defined. The origin of the right-handed global coordinate system is located at the centre of body 1 on the still water line. The x-axis is orientated positive in wave propagation direction and the z-axis is positive in upward direction. The local coordinate systems of the bodies are located in the centres of gravity of the bodies. The orientation of the local coordinate systems for the different module constellations are shown in Figure 1.

4.2 Mooring

To form an equilibrium state with the given position of the bodies, the moorings were modelled in a symmetric way. That means, the z-coordinate of the anchor points close to the tank wall were adapted to be symmetric and all moorings are modelled as linear springs with a constant stiffness and pretension. The mooring properties are shown in Table 2.

The hinge joints are positioned on deck height of the floaters at their midship section and allow a relative rotating motion around the axis parallel to the gap of the bodies.

4.3 Grid refinement

The local refinements of the numerical grid regarding the free surface were chosen in accordance with [14]. Therefore, three refinement zones were defined to capture the volume fraction transition of the free surface in Zone A, 90 % of the kinetic wave energy in Zone B and the last 9.9 % of the kinetic wave energy in Zone C. The vertical expansions of the zones are exemplary shown in Figure 3.

The vertical refinements depend on the wave amplitude whereas the refinement in wave propagation direction (x direction) depends on the wave length. The refinement in y direction is such that an aspect

Table 2: Symmetric mooring properties for field method calculations for model scale simulations

	x-coordinate of anchor point close to the tank walls (global coordinate system)			
	Single-Body [m]	Multi-Body [m]	Spring Stiffness [kN/m]	Pretension [kN]
Spring 1	2.226	2.216	13.115	3.75
Spring 2	-2.226	-2.989	13.115	3.75
Spring 3	-2.226	-2.989	13.115	3.75
Spring 4	2.226	2.216	13.115	3.75

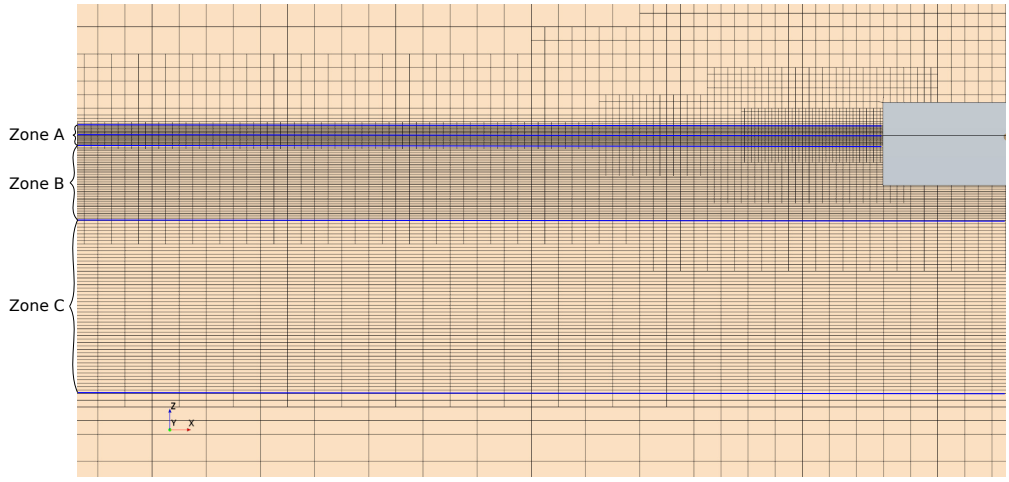

Figure 3: Local refinement of the computational grid at the free surface

ratio of 1:2 is kept for the cells. The resolution of the grid zones depending on the wave height and wave length as shown in Table 3, are kept equal for the different waves.

Table 3: Grid refinement for resolving incoming waves

	Number of cells in		
	x direction (per λ)	y direction (per λ)	z direction (per ζ_A)
Zone A	40	20	5
Zone B	20	10	-
Zone C	10	5	-

In addition, a local refinement zone around the bodies with $1.5 \cdot L_{pp}$ was chosen in order to resolve the wave generated by the body motions. L_{pp} donates 0.643 m in model scale (45 m in full scale). This results in computational meshes of 0.5 to 3 million hexahedral control volumes.
The time step was set to 0.002 sec for all model scale simulations to ensure that the Courant number is smaller than unity.

4.4 Boundary conditions

At the inlet boundary the velocity and the free surface elevation were defined according to the 5^{th} order Stokes wave theory. The hydrostatic pressure distribution was given at the outlet boundary. The hull surface and the tank walls were modelled as walls. The bottom and the top were modelled as velocity inlet boundaries. In the case of head waves for the single cuboid a symmetry boundary condition was

defined at the vertical centre plane. To account for the effect of moving boundaries mesh morphing was conducted, see [15].

5 RESULTS AND DISCUSSION

The test matrix performed for single and coupled double-body moored cuboids in regular waves comprises three different wave encounter angles and two different wave frequencies. For the multi-body cases, one wave encounter angle and two different wave frequencies were simulated. This yields six single-body, six double-body and two multi-body simulations. In the following sections, the computed motion responses for the single-body, the double-body and the multi-body cases, as shown in Table 4 , are discussed. The results are presented as computated and measured transfer functions (RAOs) of the normalized motions. The computed motion amplitudes were derived using a Discrete Fourier Transformation (DFT) of manually chosen windows of the time signals. To prevent spectral leakage in the DFT, the time window comprises six motion periods. The transversal body motions are given as the global longitudinal X-motion, transversal Y-motion and vertical Z-motion.

Table 4: Test matrix given in full scale

Test Case	Wave encounter angle [°]	Gap width [m]	Wave frequency [rad/s]	Wave amplitude [m]
TC1	180	-	0.415	0.9443
TC2	155	-	0.415	0.9443
TC3	135	-	0.415	0.9443
TC4	180	-	0.628	1.407
TC5	155	-	0.628	1.407
TC6	135	-	0.628	1.407
TC7	180	7.56	0.415	0.9443
TC8	155	7.56	0.415	0.9443
TC9	135	7.56	0.415	0.9443
TC10	180	7.56	0.628	1.407
TC11	155	7.56	0.628	1.407
TC12	135	7.56	0.628	1.407
TC13	225	7.56	0.415	0.9443
TC14	225	7.56	0.628	1.407

5.1 Single-body simulations

Overall, the computed and measured RAOs compared favourably. Figure 4 show the RAOs of the X-motion, the vertical and pitch motion for TC1 and TC 4 with the encounter angle of 180 °.

These cases were considered as symmetry cases. Therefore, a symmetry boundary condition was applied at the vertical centre plane and the transversal, roll and yaw motions were suppressed. For the nonsymmetric cases, the highest deviation between computed and measured motion amplitudes show for the roll motion. This finding was unexpected as all other motion amplitudes show a good comparison. The computed pitch motions are slightly higher for the wave frequency of 0.628 rad/s for all wave encounter angles. Given the deviation of the results for repeated model tests for wave frequency 0.628 rad/s the computed pitch amplitudes still compare favourably. Comparison of all other motion RAOs is satisfactory.

Figure 5 shows the time history of the computed and measured Z-motion for TC6. The amplitudes deviate slightly as the computed amplitude consists not only of the encounter wave frequency but has an additional low frequency influence.

The same frequency can be seen in the computed X-motion as shown in Figure 6 for TC6. Two dominant frequencies can be captured using a DFT. The encounter wave frequency and 0.0578 rad/sec

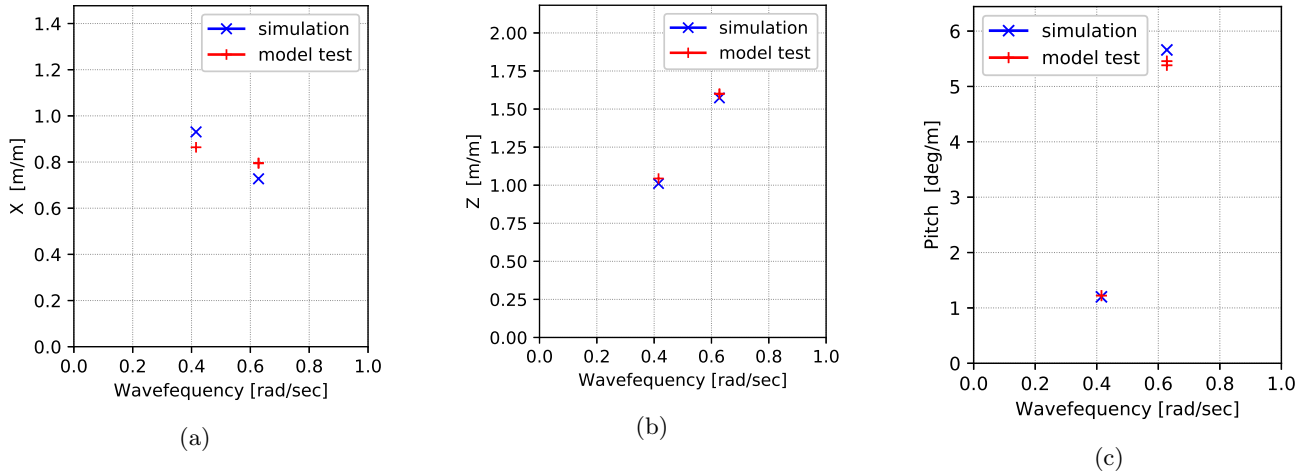

(a) (b) (c)

Figure 4: RAOs for TC1 und TC4 for X motion (a), Z motion (b) and Pitch motion (c)

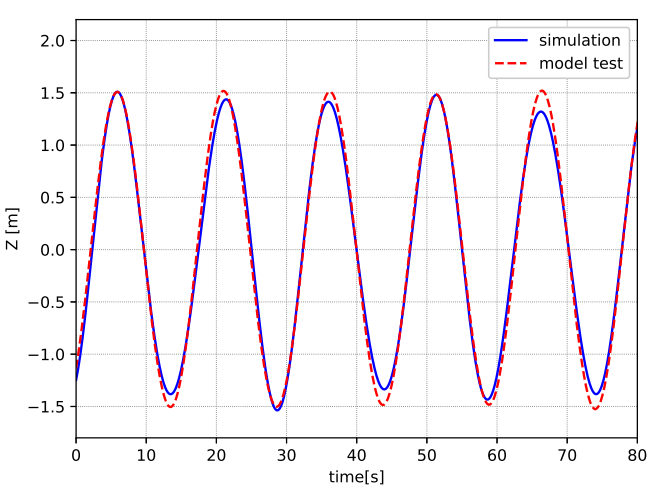

Figure 5: Time history of vertical motion for TC6

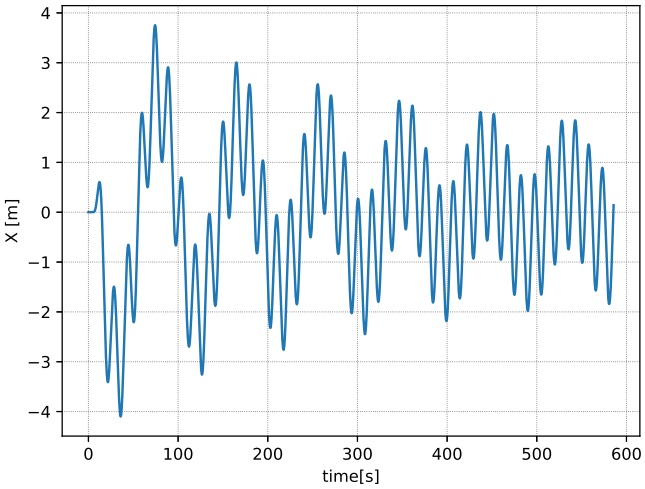

Figure 6: Time history of the horizontal X motion for TC6

caused by the mooring system. The latter is the same for surge and sway motions of all single-body computations. The amplitude of the mooring induced motion is decaying over time, as the moored system reaches a stable mooring induced motion with a constant amplitude.

5.2 Double-body simulations

Overall the computed and measured motion RAOs compare favourably. For the wave encounter angle of 135° the motion amplitudes are in a good agreement for body 2 and have slight differences in the translation motions for body 1. Figure 9 shows the horizontal X-motion for body 1 and body 2 for 135°. The deviations may be caused by the symmetry assumptions for the mooring system made for the computations or slightly erroneous measurements or computations.

For 155° wave encounter angle the vertical translation motion amplitudes are slightly smaller than the measured amplitudes for the wave frequency of 0.628 rad/s for both bodies. The transversal motion amplitude of the simulations for body 1 for the wave frequency of 0.415 rad/s is slightly higher compared to the measurements. Comparison of all other RAOs is satisfactory. The repeatability of the multi-body model tests show a bigger deviation for the test cases where repetitions were performed (for wave frequency 0.415 rad/sec). Figure 8 show the time history of the vertical motion for TC10 for body 1

and body 2. The time histories match very well for body 1. For body 2 a small phase shift between the simulations and the measurements can be seen for all simulations. The mooring induced motion in surge and sway for the multi-body cases deviates for the single-body cases as the mooring system differs. The frequency of this motion is 0.06 rad/sec for all multi-body cases.

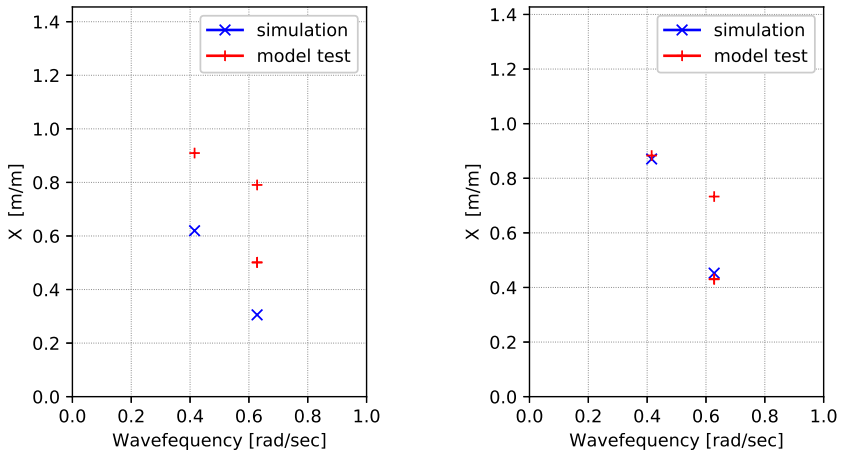

(a) (b)

Figure 7: RAOs for TC9 und TC12 for X motion for Body 1 (a) and Body 2 (b)

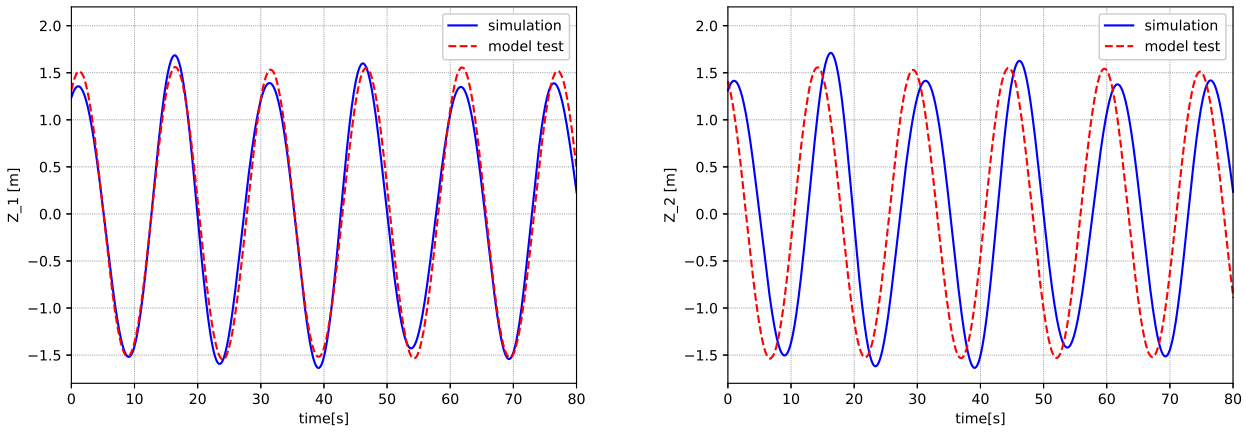

(a) (b)

Figure 8: Time history of the vertical translation motion for TC10 for body 1 (a) and body 2 (b)

5.3 Multi-body simulations

The computed and measured RAOs compare well in general. For a wave encounter frequency of 225° slight deviations for the longitudinal motion amplitudes can be seen. The computed X motion is slightly higher in all cases except for body 1 for a wave encounter frequency of 0.415 rad/s where the computed X motion amplitude is slightly smaller, as can be seen in Figure 9.

The roll motion amplitudes are matching the measured results very well except for body 3 at a wave encounter frequency of 0.638 rad/s. Comparison of all other RAOs is satisfactory. Figure 10 shows the time history of the vertical motion for TC14 for body 1, 2 and 3. The same effect of phase shifts as seen for the two body cases can be captured. The time histories match well for body 1, whereas a small phase shift can be captured for body 2 and a slightly bigger phase shift in the opposite direction is shown

for body 3. These effects are the same for all cases. The mooring induced motion in surge and sway for the multi-body cases is 0.06 rad/sec.

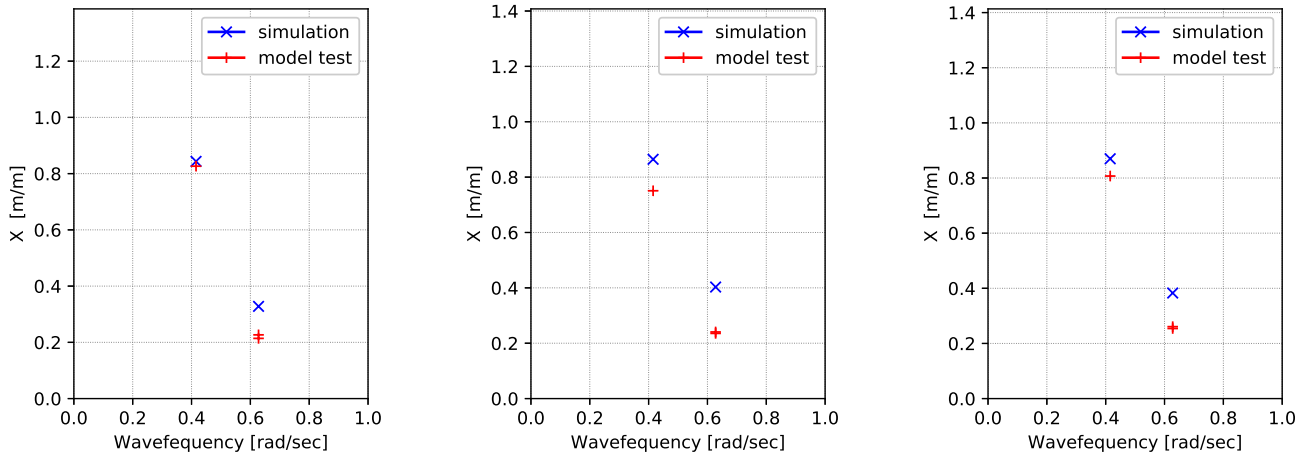

(a) (b) (c)

Figure 9: RAOs for TC13 und TC14 for X motion for Body 1(a), Body 2 (b) and Body 3 (c)

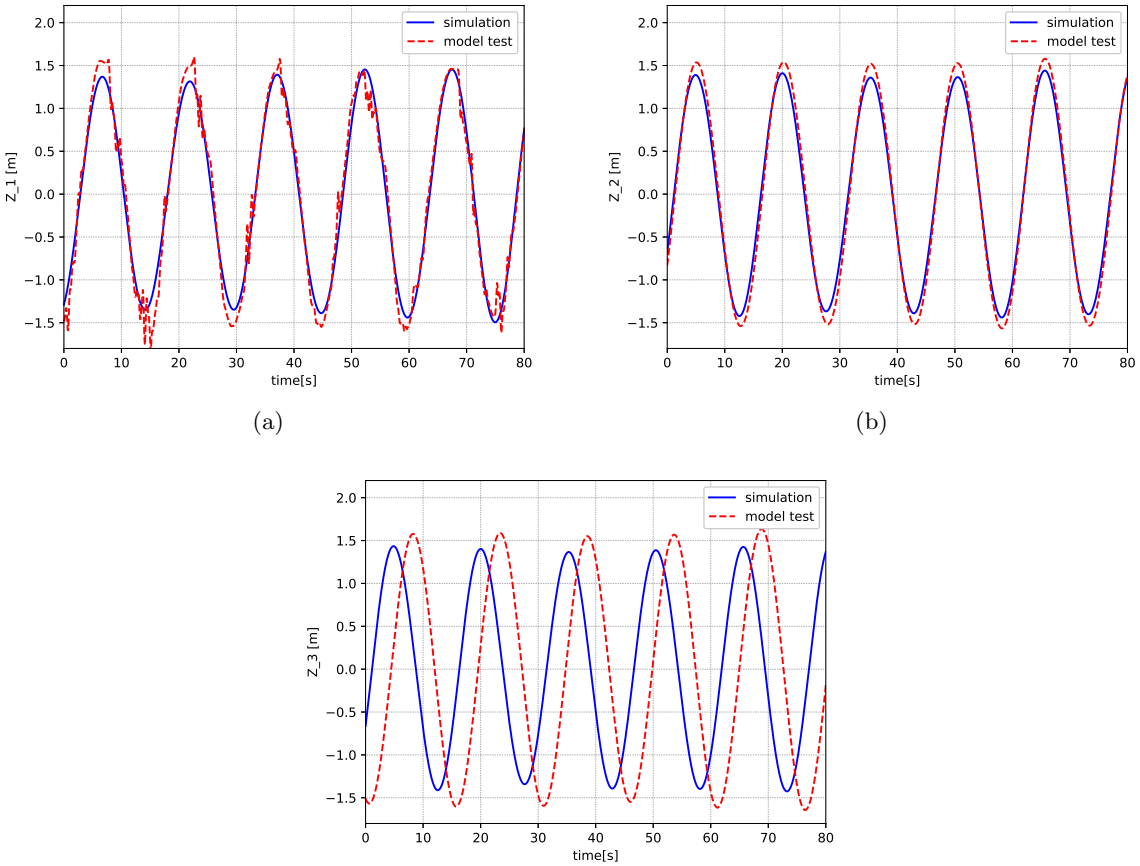

(a) (b)

(c)

Figure 10: Time history of the vertical translation motion for TC14 for body 1 (a), body 2 (b) and body 3 (c)

6 CONCLUSION

A total number of 14 simulations have been conducted for single and multiple cuboid set-ups. Overall the computed and measured motion amplitudes for these cases compare favourably. For the single-body cases some differences can be seen for the roll motion where the computed roll amplitude is smaller than the measured one. This phenomena cannot be captured for the multi-body cases where the computed roll motion amplitudes matches the measured amplitudes very well. For multi-body cases the translation motion amplitudes show slight deviations. This might be caused by slightly erroneous measurements or computations. The comparison of the time histories of the different cases show a good comparison for the single-body cases and slight phase shift differences for the multi-body cases for the different bodies. The latter might be caused by different wave propagation in the numerical grid or erroneous measurements. Despite the overall favourable comparison of the computed and measured results an extensive further investigation of the temporal and spatial discretization is planned in the future to get inside of the uncertainties of the simulations. Further investigations of viscous effects will be conducted in the future by using a viscous flow solver, based on Reynolds-Averaged Navier Stokes Equations.

ACKNOWLEDGEMENTS

This results are out of the Space@Sea project which is funded by the Horizon 2020 research and innovation program of the European Union, under the grant agreement no. 774253.

REFERENCES

[1] I. Diamantoulaki and D. C. Angelides. "Analysis of performance of hinged floating breakwaters". In: *Engineering Structures* 32.8 (2010), pp. 2407–2423.

[2] E. Loukogeorgaki, C. Michailides and D. C. Angelides. "Hydroelastic analysis of a flexible mat-shaped floating breakwater under oblique wave action". In: *Journal of Fluids and Structures* 31 (2012), pp. 103–124.

[3] C. Ji, Y. Cheng, J. Cui, Z. Yuan and O. Gaidai. "Hydrodynamic performance of floating breakwaters in long wave regime: An experimental study". In: *Ocean Engineering* 152 (2018), pp. 154–166.

[4] C. Michailides. "Power performance and dynamic response of the WLC wave energy converter based on hydroelastic analysis". In: *International Journal of Marine Energy* 19 (2017), pp. 83–94.

[5] Z. Tajali and M. Shafieefar. "Hydrodynamic analysis of multi-body floating piers under wave action". In: *Ocean Engineering* 38.17-18 (2011), pp. 1925–1933.

[6] H. Zhang, D. Xu, S. Xia, C. Lu, E. Qi, C. Tian and Y. Wu. "Nonlinear network modeling of multi-module floating structures with arbitrary flexible connections". In: *Journal of Fluids and Structures* 59 (2015), pp. 270–284.

[7] Z. Cheng, Z. Gao and T. Moan. "Wave load effect analysis of a floating bridge in a fjord considering inhomogeneous wave conditions". In: *Engineering Structures* 163 (2018), pp. 197–214.

[8] Z. Cheng, Z. Gao and T. Moan. "Hydrodynamic load modeling and analysis of a floating bridge in homogeneous wave conditions". In: *Marine Structures* 59 (2018), pp. 122–141.

[9] J. H. Ferziger and M. Peric. *Computational methods for fluid dynamics*. Springer Science & Business Media, 2012.

[10] O. El Moctar, J. Ley, J. Oberhagemann and T. Schellin. "Nonlinear computational methods for hydroelastic effects of ships in extreme seas". In: *Ocean Engineering* 130 (2017), pp. 659–673.

[11] J. Brunswig and O. El Moctar. "Prediction of ship motions in waves using RANSE". In: *Proc. 7th Numerical Towing Tank Symposium*. 2004, pp. 9–13.

[12] R. Featherstone. *Rigid body dynamics algorithms*. Springer, 2014.

[13] R. P. C.Thill. *Model tests report*. Tech. rep. TU Delft, 2018.

[14] S. Rapuc, P. Creppier, F. Jaouen and P. Regnier. "Towards guidlines for consistent wave propagation in CFD simulations". In: *NAV* (2018).

[15] H. Jasak. "Dynamic mesh handling in OpenFOAM". In: *47th AIAA Aerospace Sciences Meeting Including the New Horizons Forum and Aerospace Exposition*. 2009, p. 341.